 CMES, vol.35, no.1, pp.49-71, 2008

Inverse Scatterer Reconstruction in a Halfplane Using Surficial SH Line Sources

C. Jeong[1] **and L.F. Kallivokas**[2]

Abstract: We discuss the inverse scattering problem of identifying the shape and location of a rigid scatterer fully buried in a homogeneous halfplane, when illuminated by surficial (line) wave sources generating SH waves. To this end, we consider the full-waveform response of the coupled host-obstacle system in the frequency domain, and employ the apparatus of partial-differential-equation-constrained optimization, augmented with total differentiation for tracking shape evolutions across inversion iterations, and specialized continuation schemes in lieu of formal regularization. We report numerical results that provide evidence of algorithmic robustness for detecting a variety of shapes, including elliptically- and kite-shaped obstacles.

Keyword: Inverse scattering; buried object detection; PDE-constrained optimization; SH waves; continuation schemes

1 Introduction

Fueled, on one hand, by the desire for the non-invasive or non-destructive condition assessment of either engineered or natural/biological systems, and on the other hand, aided by the proliferation of sensors and associated technologies that enrich sensory information, interest in the solution of inverse problems has been steadily increasing in the last few years. Notwithstanding the inherent algorithmic difficulties associated with all inverse problems (e.g. solution multiplicity), the ubiquitous presence of ever increasing computational power has also conspired in broadening the application domains: from material identification (e.g. Wu, Al-Khoury, Kasbergen, Liu, and Scarpas (2007); Tabrez, Mitra, and Gopalakrishnan (2007); Harris, Mustata, Elliott, Ingham, and Lesnic (2008)) and source identification problems

[1] Department of Civil, Architectural and Environmental Engineering, The University of Texas at Austin, Austin, TX, USA

[2] Department of Civil, Architectural and Environmental Engineering, The University of Texas at Austin, Austin, TX, USA

(Huang and Shih (2007)) with applications to the civil infrastructure, to medical applications (Marin, Power, Bowtell, Sanchez, Becker, Glover, and Jones (2008)), as well as to theoretical studies of algorithmic stability of various inverse solution schemes (Noroozi, Sewell, and Vinney (2006); Ling and Atluri (2008); Ling and Takeuchi (2008)).

In a specialized class of inverse scattering problems, interest is focused on the detection of location and shape of an obstacle embedded within a contrasting background host. The localization and shape reconstruction is usually driven by scant measurements of the response of the host-obstacle system to probing waves. Application domains vary widely, and include without being limited to, the health monitoring of the civil infrastructure, geotechnical site characterization needs, medical imaging, military applications (e.g. unexploded ordnances), archaeology, and others.

A typical approach to solving the inverse problem hinges on the minimization of a misfit functional in the least-squares sense, usually defined as the difference between measured and computed responses, where the latter are obtained for trial locations and shapes of the sought scatterer. The fidelity, or even the success, of the inversion process depends greatly on the richness or completeness of the available information (measurements, boundary conditions, etc), while the source information, the background host's properties, and the material contrast between the host and sought scatterer are considered known. A considerable body of the published literature has been devoted to inverse problems where the sensors circumscribe the scatterer, and therefore offer near-complete information (in a finite-dimensional sense; see, for example, reviews by Colton and Kress (1983); Kirsch (1996); Colton and Kress (1998)). In the presence, however, of incomplete information, the inverse problem is plagued by the usual difficulties arising from ill-posedness, including solution multiplicity and ill-conditioning of the numerical processes. In such cases, regularization schemes aiming at the incorporation of *a priori* information are usually called upon to alleviate the difficulties. Moreover, classical nonlinear optimization algorithms require the repeated computation of the gradient of the misfit functional with respect to the design variables –the shape parameters in our case. An alternative, and rather elegant approach that bypasses the ill-conditioning associated with the finite-difference-based computation of the misfit gradients, is rooted in adjoint formulations. In the context of three-dimensional acoustics and elastodynamics applications, much of the background for adjoint formulations using integral equations or boundary elements has been provided by Bonnet and Guzina (see Bonnet (1995); Guzina, Fata, and Bonnet (2003); Fata, Guzina, and Bonnet (2003)).

In recent work in two dimensions (Na and Kallivokas (2008)) we discussed a

partial-differential-equation-constrained optimization approach, borrowing from the general framework laid by Lions (Lions (1971)), to cast the inversion problem in a manner similar to, but not treated by, the adjoint formulation presented in Bonnet (1995). To alleviate solution multiplicity we have also proposed and used (Na (2006); Na and Kallivokas (2009, 2008)), continuation schemes that seem to lend much needed robustness to the inversion process. The schemes can be used either in lieu of, or in combination with, standard regularization schemes. Here we extend the fullplane case to the halfplane case when the probing is driven by line SH sources (Jeong (2006)): the problem is of practical interest to underground investigations, with military and archaeological applications involving subterranean structures being of primary interest. In addition, we use the apparatus of total differentiation to account for evolving shapes during inversion iterations, and boundary elements to resolve the ensuing state and adjoint boundary value problems.

2 The forward problem

2.1 The boundary value problem

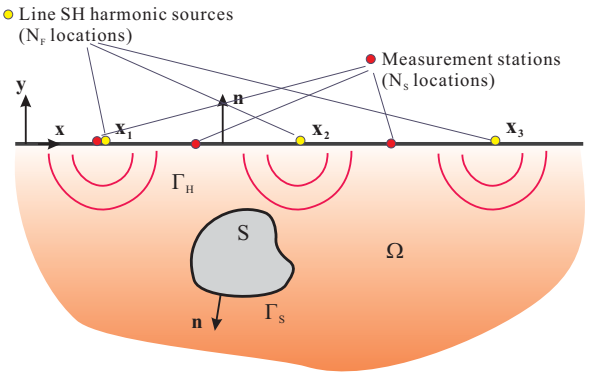

Figure 1: Prototype problem schematic: scatterer S fully embedded within semi-infinite domain Ω, illuminated by surficial line SH sources

We consider the prototype problem depicted in Fig. 1: let Ω denote the negative halfplane occupied by a linear elastic solid characterized by a shear wave velocity c_s, and let S denote a rigid scatterer bounded by Γ_S and fully embedded within Ω. The host-scatterer system is subjected to surface harmonic excitation on Γ_H, characterized by a circular frequency ω. We are concerned with the particular case of antiplane motion, i.e., of scalar SH waves generated by idealized line sources situated at x_j locations, where $j = 1,\ldots,N_F$ (point sources in two dimensions).

The associated boundary value problem, in the frequency domain, can be cast as:

$$\Delta u^{\mathrm{t}}(x) + k^2 u^{\mathrm{t}}(x) = 0, \quad x \in \hat{\Omega}, \tag{1}$$

$$u^{\mathrm{t}}(x) = 0, \quad x \in \Gamma_{\mathrm{S}}, \tag{2}$$

$$\mu \frac{\partial u^{\mathrm{t}}}{\partial n}(x) = \sum_{j=1}^{N_F} P_j \, \Delta_D(x - x_j), \quad x \in \Gamma_{\mathrm{H}}, \tag{3}$$

$$\lim_{r\to\infty} \sqrt{r} \left(\frac{\partial u^{\mathrm{t}}}{\partial r} - iku^{\mathrm{t}} \right) = 0, \tag{4}$$

where a time-harmonic factor $e^{-i\omega t}$ has been assumed throughout. In the above, $\hat{\Omega} = \Omega \setminus S$, Δ is the Laplacian, and (1) is the Helmholtz equation; u^{t} denotes the total displacement field; $k = \frac{\omega}{c_s}$ is the wavenumber; (2) is the boundary condition on the immovable rigid scatterer; (3) describes the boundary condition on the free surface Γ_{H}, with P denoting the traction amplitude, Δ_D the Dirac delta function, and n the outward normal to Γ_{H}; μ is the shear modulus of the host material; and (4) is the Sommerfeld radiation condition, where r denotes radial distance from the scatterer. If the incident field generated by the surficial sources and in the absence of the scatterer is denoted by u^{i}, then the total displacement field is given as:

$$u^{\mathrm{t}} = u^{\mathrm{i}} + u^{\mathrm{s}}, \tag{5}$$

where u^{s} denotes the scattered displacement field. Notice that the incident field generated by the surficial sources can be obtained as a solution to the following boundary value problem:

$$\Delta u^{\mathrm{i}}(x) + k^2 u^{\mathrm{i}}(x) = 0, \quad x \in \Omega, \tag{6}$$

$$\mu \frac{\partial u^{\mathrm{i}}}{\partial n}(x) = \sum_{j=1}^{N_F} P_j \Delta_D(x - x_j), \quad x \in \Gamma_{\mathrm{H}}, \tag{7}$$

$$\lim_{r\to\infty} \sqrt{r} \left(\frac{\partial u^{\mathrm{i}}}{\partial r} - iku^{\mathrm{i}} \right) = 0. \tag{8}$$

2.2 The boundary integral solution

Next, we seek solutions to the two boundary value problems (1)-(4) and (6)-(8), respectively. To this end, we favor classical boundary integral formulations, for the combined benefits of dimensionality-reduction and *a priori* satisfaction of the radiation condition they offer. Accordingly, we use Green's second identity, to arrive at the integral representation of the solution to (1)-(4):

$$u^{\mathrm{t}}(x) = -\mathfrak{D}[u^{\mathrm{t}}](x) + \mathfrak{S}\left[\frac{\partial u^{\mathrm{t}}}{\partial n}\right](x) - \sum_{j=1}^{N_F} \frac{P_j}{\mu} G^{\mathrm{H}}(x, x_j), \quad x \in \hat{\Omega}, \tag{9}$$

where the single- and double-layer potentials $\mathfrak{S}$ and $\mathfrak{D}$ are defined, respectively, as[1]:

$$\mathfrak{S}[f](x) = \int_{\Gamma_S} f(y)\, G^H(x,y)\, d\Gamma_S(y), \tag{10}$$

$$\mathfrak{D}[f](x) = \int_{\Gamma_S} f(y)\, \frac{\partial G^H(x,y)}{\partial n_y}\, d\Gamma_S(y), \tag{11}$$

with $x \in \hat{\Omega},\ y \in \Gamma_S$, and the normal n on Γ_S pointing to the interior of $\hat{\Omega}$. In the above, G^H denotes the halfplane Green's function (derived using a traction-free surface condition), which is defined as:

$$G^H(x,y) = G(x,y) + G(\hat{x},y) = -\frac{i}{4}\left(H_0^{(1)}(kr) + H_0^{(1)}(k\hat{r})\right), \tag{12}$$

where G(x,y) denotes the fullplane Green's function; $r = |x-y|$ and $\hat{r} = |\hat{x}-y|$; $\hat{x}$ denotes the mirror point of x with respect to the free surface; i is the imaginary unit; and $H_0^{(1)}(\cdot)$ is the zeroth order Hankel function of the first kind. Moreover, the following jump conditions hold:

$$\lim_{\Omega \ni x \to x \in \Gamma_S} \mathfrak{S}[f](x) = S[f](x), \text{ or } \mathfrak{S}[f] = S[f], \tag{13}$$

$$\lim_{\Omega \ni x \to x \in \Gamma_S} \mathfrak{D}[f](x) = \frac{1}{2} f(x) + D[f](x), \text{ or } \mathfrak{D}[f] = \frac{1}{2} f + D[f], \tag{14}$$

where,

$$S[f](x) = \int_{\Gamma_S} f(y)\, G^H(x,y)\, d\Gamma_S(y),\ x,y \in \Gamma_S, \tag{15}$$

$$D[f](x) = \int_{\Gamma_S} f(y) \frac{\partial G^H(x,y)}{\partial n_y} d\Gamma_S(y),\ x,y \in \Gamma_S. \tag{16}$$

By virtue of the jump conditions (13)-(14), and the boundary condition (2), Eq. 9 reduces to:

$$S\left[\frac{\partial u^t}{\partial n}\right](x) = \sum_{j=1}^{N_F} \frac{P_j}{\mu} G^H(x,x_j), \quad x \in \Gamma_S. \tag{17}$$

Equation (17) provides readily the solution for $\frac{\partial u^t}{\partial n}$ on Γ_S. To obtain the total displacement within $\hat{\Omega}$ we use the domain integral representation:

$$u^t(x) = \mathfrak{S}\left[\frac{\partial u^t}{\partial n}\right](x) - \sum_{j=1}^{N_F} \frac{P_j}{\mu} G^H(x,x_j),\ x \in \hat{\Omega}. \tag{18}$$

[1] Euler script letters (e.g. $\mathfrak{S}$) are used for domain representations of the layers, (i.e., when $x \in \hat{\Omega}$) and roman letters (e.g. S) for their boundary counterparts (i.e., when $x \in \Gamma_S$).

Similarly, it can be easily shown that the solution to (6)-(8) yields the incident field as:

$$u^{\mathrm{i}}(x) = -\sum_{j=1}^{N_F} \frac{P_j}{\mu} G^{\mathrm{H}}(x, x_j), \quad x \in \hat{\Omega}. \tag{19}$$

Consequently, the scattered field in $\hat{\Omega}$ is obtained as:

$$u^{\mathrm{s}}(x) = u^{\mathrm{t}} - u^{\mathrm{i}} = \mathfrak{S}\left[\frac{\partial u^{\mathrm{t}}}{\partial n}\right](x), \quad x \in \hat{\Omega}. \tag{20}$$

3 The inverse problem

We are concerned with the reconstruction of Γ_{S}, when given a set of measurements of the scattered displacement field at N_S locations on the surface of the halfplane (Fig. 1).

3.1 The amplitude-based misfit functional

Our starting point (see also Na and Kallivokas (2008)) is an amplitude-based misfit between the measured response and a computed response, with the latter corresponding to an estimate of the location and shape of the scatterer S. In Na and Kallivokas (2009, 2008) we argued in favor of an amplitude-based misfit as opposed to the amplitude of the difference between the two responses, since the former presents the optimizer with a less oscillatory functional than the latter, thus facilitating the search for a minimum. Accordingly, let:

$$\mathscr{L}(u^{\mathrm{t}}) = \frac{1}{2} \sum_{j=1}^{N_s} \frac{\left(|u^{\mathrm{t}}(x_j, \xi)| - |u^{\mathrm{t}}_{\mathrm{m}}(x_j)|\right)^2}{|u^{\mathrm{t}}_{\mathrm{m}}(x_j)|^2}, \tag{21}$$

where u^{t} is the scattered computed displacement based on an estimate for Γ_{S}; $u^{\mathrm{t}}_{\mathrm{m}}$ is the measured scattered displacement field due to the true scatterer. Here, we generate $u^{\mathrm{t}}_{\mathrm{m}}$ synthetically, typically using denser discretizations than those used for the inversion process in order to avoid committing classical "inverse crimes."

3.2 The augmented misfit functional

To tackle the inversion, we adopt, similarly to the fullplane case (Na and Kallivokas (2008)), a partial-differential-equation-constrained optimization approach, whereby the governing equations and associated boundary conditions are imposed as side constraints to the misfit (21) via the use of Lagrange multipliers. In this manner, the, originally, constrained optimization problem is cast as an unconstrained

one. There results:

$$\begin{aligned}\mathscr{A}(u^{\mathrm{t}},\lambda,\xi)=&\frac{1}{2}\sum_{j=1}^{N_s}\frac{\left(|u^{\mathrm{t}}(x_j,\xi)|-|u^{\mathrm{t}}_{\mathrm{m}}(x_j)|\right)^2}{|u^{\mathrm{t}}_{\mathrm{m}}(x_j)|^2}+\Re e\Big\{\\&\int_{\Omega^\xi}\lambda(x^\xi,\xi)\left[\Delta u^{\mathrm{t}}(x^\xi,\xi)+k^2u^{\mathrm{t}}(x^\xi,\xi)\right]\mathrm{d}\Omega^\xi\\&-\int_{\Gamma^\xi}\lambda_D(x^\xi,\xi)\,u^{\mathrm{t}}(x^\xi,\xi)\,\mathrm{d}\Gamma^\xi\\&-\int_{\Gamma_{\mathrm{H}}}\lambda(x^\xi,\xi)\left[\frac{\partial u^{\mathrm{t}}}{\partial n}(x^\xi,\xi)-\sum_{i=1}^{N_F}\frac{P_i}{\mu}\Delta_D(x-x_i)\right]\mathrm{d}\Gamma_{\mathrm{H}}\\&-\int_{\Gamma_\infty}\lambda(x^\xi,\xi)\left[\frac{\partial u^{\mathrm{t}}}{\partial r}(x^\xi,\xi)-iku^{\mathrm{t}}(x^\xi,\xi)\right]\mathrm{d}\Gamma_\infty\Big\}.\end{aligned}\tag{22}$$

In (22), λ denotes Lagrange multiplier; λ_D also denotes a Lagrange multiplier used to enforce the essential boundary condition on the scatterer's boundary (λ and λ_D have different physical dimensions). The scalar metric ξ above has been introduced to account for the evolution of the scatterer boundary during the search iterations for the true shape Γ_{S}. The idea originated from the work of Guzina and Bonnet (Guzina, Fata, and Bonnet (2003)), where it was similarly used. In this sense, ξ depends on the parameterization of every trial shape. Thus, Γ^ξ denotes one snapshot of Γ_{S}, which, in general, differs from the true Γ_{S}. Notice also that, since Γ^ξ changes, so does the surrounding domain: we use Ω^ξ to denote the, also evolving, semi-infinite domain surrounding Γ^ξ.

To reconstruct Γ_{S} based on the measurements $u^{\mathrm{t}}_{\mathrm{m}}$, we seek a stationary point for the augmented functional $\mathscr{A}$. To this end, it is necessary that first-order optimality conditions for $\mathscr{A}$ be satisfied. The variations of $\mathscr{A}$ with respect to the scalar metric ξ require the apparatus of total differentiation (Petryk and Mróz (1986); Kosinski (1986)), for which we repeat below the primary ingredients.

3.3 The evolving scatterer shape

We consider that the boundary evolves driven by a transformational velocity field v, which, in general, can be described by two components, one normal and one tangential to the boundary. For small shape perturbations, that is, as long as the step changes across shape iterations remain small, the tangential velocity component can be ignored. Thus, if x denotes a point on boundary Γ (Fig. 2), then, driven by the velocity component v_n, Γ evolves to Γ^ξ, and x becomes:

$$\Gamma\ni x\to x+\xi v_n(x)n(x)\equiv x^\xi\in\Gamma^\xi,\tag{23}$$

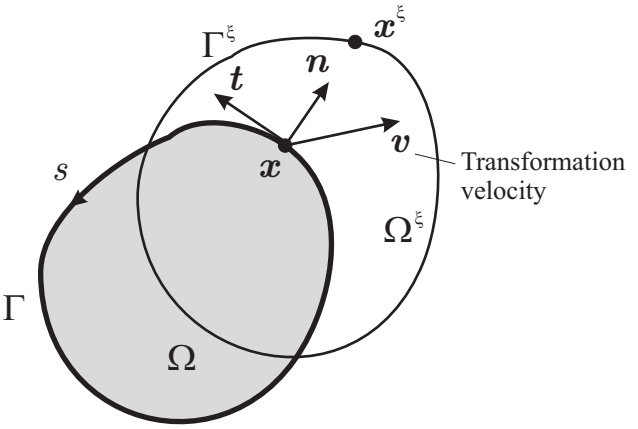

Figure 2: Boundary shape evolution due to a transformational velocity field

where n is the normal to the boundary. Accordingly, when v_n is known, all that is needed to characterize the shape evolution is the scalar metric ξ. Notice that Γ corresponds to $\xi = 0$. To be able to accommodate the variations of the augmented functional $\mathscr{A}$ with respect to ξ, the following total derivatives of a scalar field, line, and domain integrals, are needed (Petryk and Mróz (1986); Kosinski (1986)):

$$\left[\frac{Df(x^\xi,\xi)}{D\xi}\right]_{\xi=0} = \left[\dot{f} + v_n \frac{\partial f}{\partial n}\right], \tag{24}$$

$$\left[\frac{D}{D\xi}\int_{\Gamma^\xi} f(x^\xi,\xi)\,\mathrm{d}\Gamma^\xi\right]_{\xi=0} = \int_\Gamma \left[\dot{f} + v_n \frac{\partial f}{\partial n} - \kappa f v_n\right]\mathrm{d}\Gamma, \tag{25}$$

$$\left[\frac{D}{D\xi}\int_{\Omega^\xi} f(x^\xi,\xi)\,\mathrm{d}\Omega^\xi\right]_{\xi=0} = \int_\Omega \dot{f}\,\mathrm{d}\Omega + \int_\Gamma f\, v_n\,\mathrm{d}\Gamma, \tag{26}$$

where κ denotes the curvature of the boundary Γ, and $\dot{f} = \frac{\partial f}{\partial \xi}$.

3.4 The first-order optimality conditions

The first-order optimality conditions are established by calculating the first variations of the augmented functional, $\mathscr{A}$, with respect to the Lagrange multipliers (or adjoint variables) λ, λ_D, the state variable u^{t}, and the scalar metric ξ. Accordingly:

$$\delta_\lambda \mathscr{A} = 0, \quad \delta_{\lambda_D}\mathscr{A} = 0, \quad \delta_{u^{\mathrm{t}}}\mathscr{A} = 0, \quad \delta_\xi \mathscr{A} = 0. \tag{27}$$

3.4.1 The first condition

Imposing the first of (27) yields:

$$\delta_\lambda \mathscr{A} = \Re e \left\{ \int_{\Omega^\xi} \delta\lambda \, (\Delta u^{\mathrm{t}} + k^2 u^{\mathrm{t}}) \, \mathrm{d}\Omega^\xi - \int_{\Gamma_{\mathrm{H}}} \delta\lambda \left(\frac{\partial u^{\mathrm{t}}}{\partial n} - \sum_{i=1}^{N_F} \frac{P_i}{\mu} \Delta_D(x - x_i) \right) \mathrm{d}\Gamma_{\mathrm{H}} \right.$$
$$\left. - \int_{\Gamma_\infty} \delta\lambda \left(\frac{\partial u^{\mathrm{t}}}{\partial r} - iku^{\mathrm{t}} \right) \mathrm{d}\Gamma_\infty \right\} = 0, \tag{28}$$

$$\delta_{\lambda_D} \mathscr{A} = \Re e \left\{ - \int_{\Gamma^\xi} \delta\lambda_D \, u^{\mathrm{t}} \, \mathrm{d}\Gamma^\xi \right\} = 0. \tag{29}$$

Clearly, for arbitrary $\delta\lambda$ and $\delta\lambda_D$, the vanishing of the variations in (28) and (29) recovers the forward (or state) problem (1)-(4) for any instantiation of Γ^ξ and Ω^ξ. The solution of the state problem is then readily recoverable by using the boundary integral equation (17).

3.4.2 The second condition

Next, we take variations of $\mathscr{A}$ with respect to the state variables u^{t}. There results:

$$\delta_{u^{\mathrm{t}}} \mathscr{A} = \Re e \left\{ \sum_{j=1}^{N_s} \delta u^{\mathrm{t}}(x_j) \frac{\bar{u^{\mathrm{t}}}(x_j)}{|u^{\mathrm{t}}_{\mathrm{m}}(x_j)|^2} \left(1 - \frac{|u^{\mathrm{t}}_{\mathrm{m}}(x_j)|}{|u^{\mathrm{t}}(x_j)|} \right) \right.$$
$$+ \int_{\Omega^\xi} \delta u^{\mathrm{t}} (\Delta\lambda + k^2\lambda) \mathrm{d}\Omega^\xi - \int_{\Gamma^\xi} \delta u^{\mathrm{t}} \left(\lambda_D - \frac{\partial\lambda}{\partial n} \right) \mathrm{d}\Gamma^\xi$$
$$- \int_{\Gamma^\xi} \lambda \frac{\partial \delta u^{\mathrm{t}}}{\partial n} \mathrm{d}\Gamma^\xi - \int_{\Gamma_{\mathrm{H}}} \delta u^{\mathrm{t}} \frac{\partial\lambda}{\partial n} \mathrm{d}\Gamma_{\mathrm{H}}$$
$$\left. - \int_{\Gamma_\infty} \delta u^{\mathrm{t}} \left(\frac{\partial\lambda}{\partial n} - ik\lambda \right) \mathrm{d}\Gamma_\infty \right\} = 0, \tag{30}$$

where an overbar ($\bar{u^{\mathrm{t}}}$) denotes complex conjugate of the subtended variable. For (30) to be satisfied for arbitrary δu^{t} and $\frac{\partial \delta u^{\mathrm{t}}}{\partial n}$, the adjoint variables λ and λ_D should satisfy the following:

Adjoint problem:

$$\Delta\lambda(x)+k^2\lambda(x)=-\sum_{j=1}^{N_s}\frac{\bar{u^{\mathrm{t}}}(x)}{|u^{\mathrm{t}}_{\mathrm{m}}(x_j)|^2}\left(1-\frac{|u^{\mathrm{t}}_{\mathrm{m}}(x_j)|}{|u^{\mathrm{t}}(x)|}\right)\Delta_D(x-x_j), x\in\Omega^{\xi},$$

$$\lambda(x)=0,\quad \lambda_D(x)=\frac{\partial\lambda}{\partial n},\quad x\in\Gamma^{\xi},$$

$$\frac{\partial\lambda}{\partial n}(x)=0,\quad x\in\Gamma_{\mathrm{H}},$$

$$\lim_{r\to\infty}\sqrt{r}\left(\frac{\partial\lambda}{\partial r}-ik\lambda\right)=0. \tag{31}$$

We remark that the governing operator in the adjoint problem (31) is identical to the governing operators in the state problem, and thus a single matrix inversion is sufficient for both the state and adjoint problems. Thus, we use the following boundary integral equation to solve for $\frac{\partial\lambda}{\partial n}$ on Γ^{ξ}:

$$S\left[\frac{\partial\lambda}{\partial n}\right](x)=\sum_{j=1}^{N_s}G^{\mathrm{H}}(x,x_j)\frac{\bar{u^{\mathrm{t}}}(x_j)}{|u^{\mathrm{t}}_{\mathrm{m}}(x_j)|^2}\left(1-\frac{|u^{\mathrm{t}}_{\mathrm{m}}(x_j)|}{|u^{\mathrm{t}}(x_j)|}\right),\ x\in\Gamma^{\xi}. \tag{32}$$

Notice again that the single-layer terms in (17) and (32) are the same for both the state and adjoint problems.

3.4.3 The third condition

Next, we require that the variation of $\mathscr{A}$ with respect to ξ vanish:

$$\delta_{\xi}\mathscr{A}=\frac{D}{D\xi}\left[\frac{1}{2}\sum_{j=1}^{N_s}\frac{\left(|u^{\mathrm{t}}(x_j,\xi)|-|u^{\mathrm{t}}_{\mathrm{m}}(x_j)|\right)^2}{|u^{\mathrm{t}}_{\mathrm{m}}(x_j)|^2}\right.$$

$$+\Re e\left\{\int_{\Omega^{\xi}}\lambda(\Delta u^{\mathrm{t}}+k^2u^{\mathrm{t}})\mathrm{d}\Omega^{\xi}-\int_{\Gamma^{\xi}}\lambda_D\,u^{\mathrm{t}}\,\mathrm{d}\Gamma^{\xi}\right.$$

$$\left.\left.-\int_{\Gamma_{\mathrm{H}}}\lambda\left(\frac{\partial u^{\mathrm{t}}}{\partial n}-\sum_{i=1}^{N_F}\frac{P_i}{\mu}\Delta_D(x-x_i)\right)\mathrm{d}\Gamma_{\mathrm{H}}-\int_{\Gamma_{\infty}}\lambda\left(\frac{\partial u^{\mathrm{t}}}{\partial r}-iku^{\mathrm{t}}\right)\mathrm{d}\Gamma_{\infty}\right\}\right]_{\xi=0}. \tag{33}$$

By taking into account the total derivative of a scalar field (24), and that the transformation velocity v_n vanishes on the free surface Γ_{H}, there holds:

$$\left[\frac{D}{D\xi}\left\{\frac{1}{2}\sum_{j=1}^{N_s}\frac{\left(|u^{\mathrm{t}}(x_j,\xi)|-|u^{\mathrm{t}}_{\mathrm{m}}(x_j)|\right)^2}{|u^{\mathrm{t}}_{\mathrm{m}}(x_j)|^2}\right\}\right]_{\xi=0}$$

$$=\Re e\left\{\sum_{j=1}^{N_s}\dot{u}^{\mathrm{t}}(x_j)\frac{\bar{u^{\mathrm{t}}}(x_j)}{|u^{\mathrm{t}}_{\mathrm{m}}(x_j)|^2}\left(1-\frac{|u^{\mathrm{t}}_{\mathrm{m}}(x_j)|}{|u^{\mathrm{t}}(x_j)|}\right)\right\}. \tag{34}$$

By using (34), integration by parts, i.e., that $\lambda\Delta u^{\mathrm{t}} = -\nabla\lambda\cdot\nabla u^{\mathrm{t}} + \nabla\cdot(\lambda\nabla u^{\mathrm{t}})$, and the divergence theorem, (33) becomes:

$$\begin{aligned}\delta_\xi \mathscr{A} =& \Re e\left\{\sum_{j=1}^{N_s} \dot{u}^{\mathrm{t}}(x_j)\frac{\bar{u^{\mathrm{t}}}(x_j)}{|u^{\mathrm{t}}_{\mathrm{m}}(x_j)|^2}\left(1-\frac{|u^{\mathrm{t}}_{\mathrm{m}}(x_j)|}{|u^{\mathrm{t}}(x_j)|}\right)\right\}\\ &+\frac{D}{D\xi}\left[\Re e\left\{\int_{\Omega^\xi}(-\nabla\lambda\cdot\nabla u^{\mathrm{t}}+k^2\lambda u^{\mathrm{t}})\mathrm{d}\Omega^\xi - \int_{\Gamma^\xi}\lambda\frac{\partial u^{\mathrm{t}}}{\partial n}\mathrm{d}\Gamma^\xi - \int_{\Gamma^\xi}\lambda_D\, u^{\mathrm{t}}\,\mathrm{d}\Gamma^\xi\right.\right.\\ &\left.\left.+\int_{\Gamma_{\mathrm{H}}}\lambda\sum_{i=1}^{N_F}\frac{P_i}{\mu}\Delta_D(x-x_i)\,\mathrm{d}\Gamma_{\mathrm{H}} + \int_{\Gamma_\infty}\lambda iku^{\mathrm{t}}\,\mathrm{d}\Gamma_\infty\right\}\right]_{\xi=0}. \end{aligned} \tag{35}$$

Using (24)-(26), it can be shown that the line integrals in (35) reduce to:

$$\frac{D}{D\xi}\left[\Re e\int_{\Gamma^\xi}\lambda\frac{\partial u^{\mathrm{t}}}{\partial n}\mathrm{d}\Gamma^\xi\right]_{\xi=0} = \Re e\int_{\Gamma_{\mathrm{S}}}\left[\dot{\lambda}\frac{\partial u^{\mathrm{t}}}{\partial n}+v_n\frac{\partial\lambda}{\partial n}\frac{\partial u^{\mathrm{t}}}{\partial n}\right]\mathrm{d}\Gamma_{\mathrm{S}}, \tag{36}$$

$$\frac{D}{D\xi}\left[\Re e\int_{\Gamma^\xi}\lambda_D\, u^{\mathrm{t}}\,\mathrm{d}\Gamma^\xi\right]_{\xi=0} = \Re e\int_{\Gamma_{\mathrm{S}}}\left[\lambda_D\dot{u^{\mathrm{t}}}+v_n\lambda_D\frac{\partial u^{\mathrm{t}}}{\partial n}\right]\mathrm{d}\Gamma_{\mathrm{S}}. \tag{37}$$

$$\frac{D}{D\xi}\left[\Re e\int_{\Gamma_{\mathrm{H}}}\lambda\sum_{i=1}^{N_F}\frac{P_i}{\mu}\Delta_D(x-x_i)\,\mathrm{d}\Gamma_{\mathrm{H}}\right]_{\xi=0} = \Re e\int_{\Gamma_{\mathrm{H}}}\dot{\lambda}\sum_{i=1}^{N_F}\frac{P_i}{\mu}\Delta_D(x-x_i)\,\mathrm{d}\Gamma_{\mathrm{H}} \tag{38}$$

$$\frac{D}{D\xi}\left[\Re e\int_{\Gamma_\infty}\lambda iku^{\mathrm{t}}\mathrm{d}\Gamma_\infty\right]_{\xi=0} = \Re e\int_{\Gamma_\infty} ik(\dot{\lambda u^{\mathrm{t}}})\mathrm{d}\Gamma_\infty, \tag{39}$$

where we used that v_n vanishes on both Γ_{H} and Γ_∞. Similarly, the domain integral in (35) reduces to:

$$\begin{aligned}&\frac{D}{D\xi}\left[\Re e\int_{\Omega^\xi}(-\nabla\lambda\cdot\nabla u^{\mathrm{t}}+k^2\lambda u^{\mathrm{t}})\mathrm{d}\Omega^\xi\right]_{\xi=0} =\\ &\Re e\left\{\int_{\hat{\Omega}}(-\nabla\dot{\lambda}\cdot\nabla u^{\mathrm{t}}-\nabla\lambda\cdot\nabla\dot{u^{\mathrm{t}}}+\dot{\lambda}k^2u^{\mathrm{t}}+\dot{u^{\mathrm{t}}}k^2\lambda)\mathrm{d}\hat{\Omega}+\int_{\Gamma_{\mathrm{S}}}(-\nabla\lambda\cdot\nabla u^{\mathrm{t}})v_n\mathrm{d}\Gamma_{\mathrm{S}}\right\}.\end{aligned} \tag{40}$$

Using the weak forms of the state and adjoint problems, with $\dot{\lambda}$ and $\dot{u}^{\mathrm{s}}$ as weight functions, respectively, yields:

$$\int_{\hat{\Omega}}(-\nabla\dot{\lambda}\cdot\nabla u^{\mathrm{t}}+\dot{\lambda}k^2u^{\mathrm{t}})\mathrm{d}\hat{\Omega} = \int_{\Gamma_{\mathrm{S}}}\dot{\lambda}\frac{\partial u^{\mathrm{t}}}{\partial n}\mathrm{d}\Gamma_{\mathrm{S}} - \int_{\Gamma_\infty} ik\dot{\lambda}u^{\mathrm{t}}\mathrm{d}\Gamma_\infty - \int_{\Gamma_{\mathrm{H}}}\dot{\lambda}\frac{\partial u^{\mathrm{t}}}{\partial n}\,\mathrm{d}\Gamma_{\mathrm{H}}, \tag{41}$$

$$\begin{aligned}\int_{\hat{\Omega}}(-\nabla\dot{u^{\mathrm{t}}}\cdot\nabla\lambda+\dot{u^{\mathrm{t}}}k^2\lambda)\,\mathrm{d}\hat{\Omega} =& -\sum_{j=1}^{N_s}\dot{u}^{\mathrm{t}}(x_j)\frac{\bar{u^{\mathrm{t}}}(x_j)}{|u^{\mathrm{t}}_{\mathrm{m}}(x_j)|^2}\left(1-\frac{|u^{\mathrm{t}}_{\mathrm{m}}(x_j)|}{|u^{\mathrm{t}}(x_j)|}\right)\\ &-\int_{\Gamma_\infty} ik\dot{u^{\mathrm{t}}}\lambda\,\mathrm{d}\Gamma_\infty+\int_{\Gamma_{\mathrm{S}}}\dot{u^{\mathrm{t}}}\frac{\partial\lambda}{\partial n}\,\mathrm{d}\Gamma_{\mathrm{S}}.\end{aligned} \tag{42}$$

Finally, the last integral in (40), using the gradient's decomposition into tangential and normal components, can be shown to yield:

$$\int_{\Gamma_S}(-\nabla\lambda\cdot\nabla u^t)\,v_n\,d\Gamma_S=\int_{\Gamma_S}\left(-\frac{\partial\lambda}{\partial n}\frac{\partial u^t}{\partial n}v_n\right)d\Gamma_S. \tag{43}$$

Combining (33)-(43) results in the control equation, or control problem, which is satisfied only for the true target.

Control problem:

$$\delta_\xi\mathscr{A}=\Re e\left[\int_{\Gamma_S}v_n\frac{\partial\lambda}{\partial n}\frac{\partial u^t}{\partial n}d\Gamma_S\right]=0. \tag{44}$$

4 Numerical experiments

The simultaneous solution of the state, adjoint, and control problems, ensures the stationarity of the augmented functional $\mathscr{A}$, and, therefore, lends hope to recovering the true target. Naturally, the problem is ill-posed in the Hadamard sense, and is thus prone to solution multiplicity. We discuss first the solution approach for the triad of the total displacement field u^t, the adjoint variables (or Lagrange multipliers) λ, and the shape parameters defining Γ_S.

The inversion process is initiated with a trial shape constructed via a parameterization of the scatterer's boundary Γ_S, defined by a shape parameterization function $\Psi(p)$, with p denoting shape parameters (e.g., p could denote coordinates of characteristic points such as the center of a circle or the corners of a rectangle, coefficients of a series describing the assumed shape, nodal coordinates of a boundary discretization, etc). The shape parameters p constitute the control variables. Next, we opt for a, so-called, reduced-space approach, whereby the state problem is solved first using (17) for a trial shape Γ_S, thus yielding u^t. Then, the adjoint problem is solved using (32), driven by both the measurements u^t_m and the state solution u^t obtained in the previous step. All that remains is to update the shape parameters p. This end, we note that:

$$\delta_{p_i}\mathscr{A}=\nabla_{p_i}\mathscr{L}, \tag{45}$$

where p_i denotes the i-th parameter of the shape parameter vector. Equation (45) suggests that the gradient of the (original) misfit functional with respect to a shape parameter equals the variation of the augmented functional with respect to the shape parameter, owing to the satisfaction of the side conditions, which, in turn, is due to the solution of the state and adjoint problems at the two prior steps. Furthermore:

$$\delta_{p_i}\mathscr{A}=\delta_\xi\mathscr{A}=\Re e\left[\int_{\Gamma_S}v_n^i\frac{\partial\lambda}{\partial n}\frac{\partial u^t}{\partial n}d\Gamma_S\right], \tag{46}$$

where the normal component of the transformational velocity v_n^i at a point x is defined as:

$$v_n^i(x) = \left.\frac{\partial \Psi(p)}{\partial p_i}\right|_{\text{at } x} \cdot n(x) = \frac{\partial \Psi_x}{\partial p_i} n_x + \frac{\partial \Psi_y}{\partial p_i} n_y. \tag{47}$$

In (47), Ψ_x, Ψ_y denotes the cartesian components of the shape parameterization function Ψ. Thus, by virtue of (45)-(46), any gradient-based scheme can be used to update the shape parameters p: here we used a conjugate-gradient scheme. Once the shape parameters have been updated, and thus a new trial Γ_S has been computed, the state and adjoint problems are solved anew. The process continues until the shape parameters have converged.

To alleviate solution multiplicity, and in lieu of regularization, we use a frequency continuation scheme (Na (2006); Na and Kallivokas (2009)). Accordingly, we probe at multiple frequencies, typically starting with a low frequency, and feed the converged shape parameters due to one frequency's probing as initial values for the shape parameters used during the next (higher) probing frequency. At the end of the process, we revisit all lower frequency misfits to ensure that the final shape parameters yield indeed a minimum for all frequencies. The process, thus far, has been met with success, and is characterized by robustness. Typically, we have observed that probing at low frequencies tends to localize the scatterer, whereas high frequencies tend to refine the shape.

We discuss next specific numerical experiments, where we report the convergence path of trial shapes to the target based on measurements resulting from the surficial line SH sources. To quantify how well the converged shape fits the target, we define a solution-fitness metric e_f as:

$$e_f = \frac{(A_E - A_\cap) + (A_T - A_\cap)}{A_T}, \tag{48}$$

where A_E denotes the area enclosed by the boundary of the estimated shape, whereas A_T is the area surrounded by the boundary Γ_S of the true shape; $A_\cap$ represents the area defined by the overlap between A_E and A_T.

4.1 Circular scatterer

We consider first the case of circular scatterer; the problem configuration is shown in Fig. 3. We define the shape parameterization function Ψ as:

$$\Psi(p) = \left\{ \begin{array}{l} x_0 + R\cos\theta \\ y_0 + R\sin\theta \end{array} \right\}, \tag{49}$$

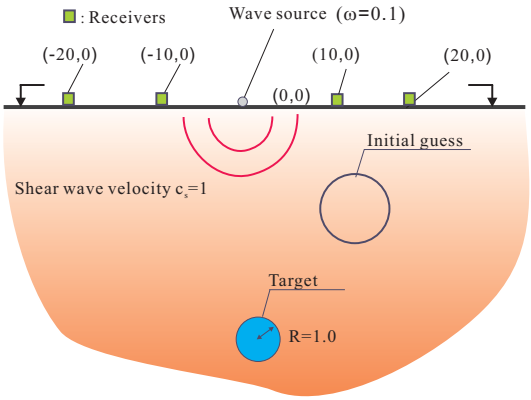

Figure 3: Circular scatterer: problem configuration

where θ ranges from 0 to 2π, and $p = [x_0, y_0, R]$; x_0 and y_0 denote the cartesian coordinates of the center of a circle of radius R. The initial guess is also a circle of radius $R = 1.5$, whose center is at (5,-4), i.e., the initial shape parameters are $p_0 = [5, -4, 1.5]$, whereas the true shape parameters are $p_{\text{true}} = [0, -10, 1]$. We use a single wave source with $\omega = 0.1$ situated at $(0, 0)$, within a medium characterized by $c_s = 1$. Four sensors, located at (-20,0), (-10,0), (10,0) and (20,0) on the free surface, are used to drive the inversion process.

As it can be seen in Fig. 4, as the iteration number increases, the shape approaches the target quite accurately. At the 645-th iteration, the shape parameters have converged to $p_{\text{final}} = [0.000, -9.987, 1.000]$, and the solution-fitness metric is reduced to 1.53% (Fig. 5).

4.2 Elliptical scatterer

Next, we turn to the case of an elliptical scatterer with a ratio of major to minor axis of 4 to 1, whose shape is parameterized using four parameters:

$$\Psi(p) = \left\{ \begin{array}{l} x_0 + a\cos\theta \\ y_0 + b\sin\theta \end{array} \right\}, \tag{50}$$

where θ ranges from 0 to 2π; $p = [x_0, y_0, a, b]$; x_0 and y_0 denote the cartesian coordinates of the center of the ellipse; and, a and b are the lengths of the major and minor semi-axis, respectively. The initial guess is a circular shape with parameters $p_0 = [-7, -2, 1, 1]$, whereas the target shape parameter vectors is $p_{\text{true}} = [2, -8, 2, 0.5]$. Figure 6 depicts the problem configuration: the sensors are located at (-15,0), (-5,0), (5,0) and (15,0), and we use three wave sources situated at (-10,0), (0,0), and (10,0)

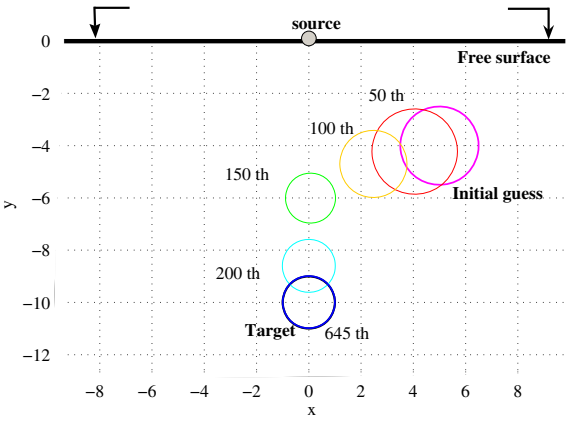

Figure 4: The circular scatterer: convergence path

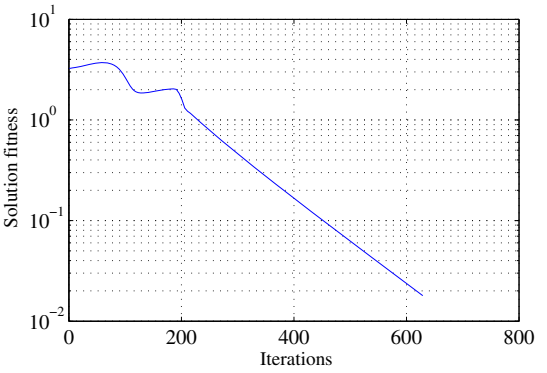

Figure 5: The circular scatterer: solution-fitness metric

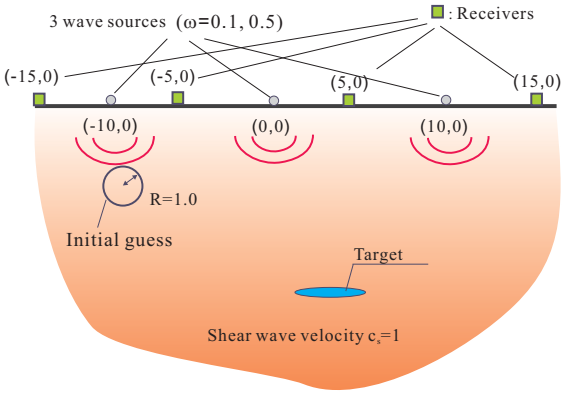

Figure 6: The elliptical scatterer: problem configuration

on the free surface. We start the inversion with a probing frequency of $\omega = 0.1$ However, as it can be seen from Fig. 7, after more than 200 iterations the process has converged without the target having been recovered. We turn to the frequency continuation scheme, and increase the probing frequency to $\omega = 0.5$, which now nicely recovers the target. The final parameters are $p_{\text{final}} = [2.01, -8.01, 1.98, 0.49]$ and the fitness metric is reduced to less than 3% (Fig. 8).

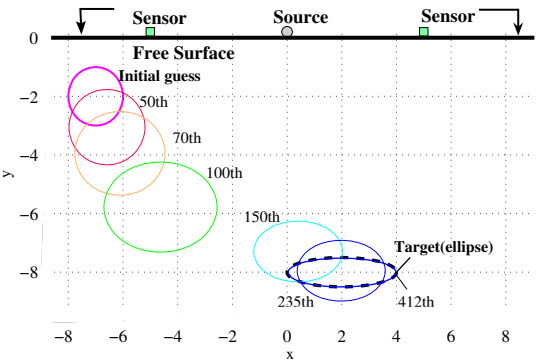

Figure 7: The elliptical scatterer: convergence path

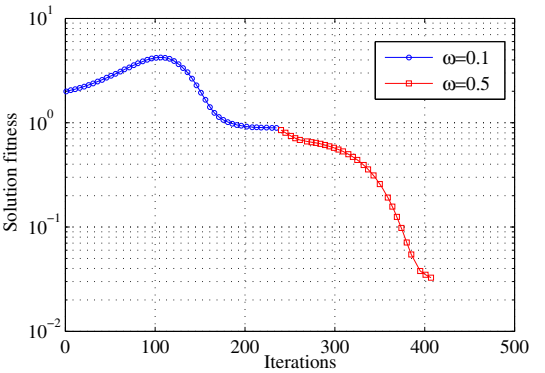

Figure 8: The elliptical scatterer: solution fitness metric

4.3 Potato-shaped scatterer

To further exercise the algorithm we turn to a mixed convex/concave shape in the form of a potato. The geometry of the scatterer is parameterized by the following

relationship between Ψ and p:

$$\Psi(p) = \left\{ \begin{array}{l} a_1 + \Big[a_3 + \sum_{i=1}^{3} \Big\{ a_{2i+2} \cos(i\theta) + \\ \qquad a_{2i+3} \sin(i\theta) \Big\} \Big] \cos(\theta) \\ a_2 + \Big[a_3 + \sum_{i=1}^{3} \Big\{ a_{2i+2} \cos(i\theta) + \\ \qquad a_{2i+3} \sin(i\theta) \Big\} \Big] \sin(\theta) \end{array} \right\}, \tag{51}$$

where θ ranges from 0 to 2π, and $p = [a_1, \ldots, a_9]$. The inversion is initiated with initial shape parameters $p_0 = [-5, -4, 1, 0, 0, 0, 0, 0, 0]$ corresponding to a circular scatterer. The target's parameters are
$p_{\text{true}} = [2, -10, 1, 0.2, -0.3, 0.125, 0.125, -0.05, -0.05]$. We deploy six sensors situated at (-30,0), (-20,0), (-10,0), (10,0), (20,0) and (30,0). The wave sources are located on the free surface at (-15,0), (0,0), and (15,0). We use the frequency-continuation scheme with probing frequencies at $\omega = 0.1$, 0.3, 0.5 and 0.8. We further enforce the shape to remain circular during the probing with the first frequency in order to facilitate localization, prior to shape refinement, and to also prevent the shape from changing in non-physical ways, for which we have not accounted in our algorithm. As it can be seen in Figure 9, using the first frequency only, the shape parameters have converged to a location near the true target. Next, we release the shape constraint and use the continuation scheme to probe at higher frequencies. As depicted in Fig. 10, the target is successfully reconstructed. Figure 11 shows the convergence of the solution-fitness metric, which is reduced to 4.6% for the final parameter set ($p_{\text{final}} = [$ 2.11, -10.21, 1.03, 0.056, -0.0096, 0.13, 0.10, -0.08, -0.022]).

4.4 The kite-shaped scatterer

We finally attempt to invert for the shape of a kite-shaped scatterer, whose exact shape is provided by the continuous parameterization below:

$$\begin{aligned} x(\theta) &= \cos\theta + 0.65(\cos 2\theta - 1), \\ y(\theta) &= 1.5 \sin\theta - 10, \end{aligned} \tag{52}$$

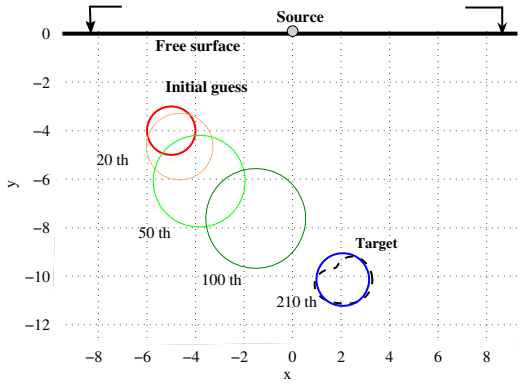

Figure 9: The potato-shaped scatterer: convergence path

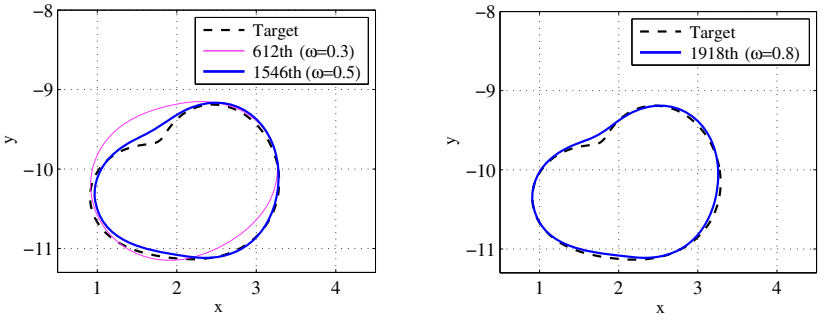

(a) $\omega = 0.3$ and 0.5 (b) $\omega = 0.8$

Figure 10: The potato-shaped scatterer: convergence stages at $\omega = 0.3, 0.5, 0.8$

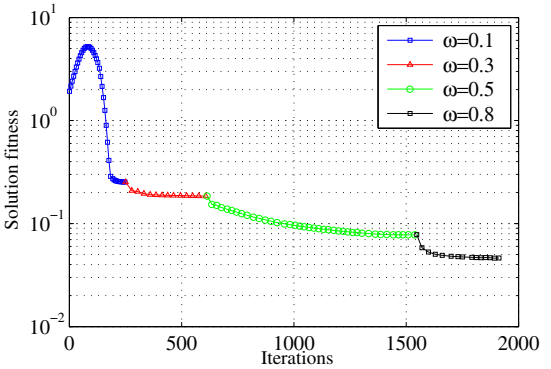

Figure 11: The potato-shaped scatterer: solution-fitness metric

where θ ranges from 0 to 2π. In order to approximate the boundary, the following boundary parameterization function is employed:

$$\Psi(p) = \left\{ \begin{array}{l} a_1 + \Big[a_3 + \sum_{i=1}^{8} \Big\{ a_{2i+2}\cos(i\theta) + \\ \qquad a_{2i+3}\sin(i\theta) \Big\} \Big] \cos(\theta) \\ a_2 + \Big[a_3 + \sum_{i=1}^{8} \Big\{ a_{2i+2}\cos(i\theta) + \\ \qquad a_{2i+3}\sin(i\theta) \Big\} \Big] \sin(\theta) \end{array} \right\}, \tag{53}$$

where again θ ranges from 0 to 2π, and $p = [a_1, \ldots, a_{19}]$. We start again the inversion with the shape parameters $p_0 = [-6, -3, 1, 0, \cdots, 0]$ corresponding to a circular scatterer. We remark that, as it can be seen in the first of the convergence graphs shown in Fig. 12 the kite-shaped scatterer has deeper concave parts than the preceding shape, and thus represents a more severe test. We, therefore, use a greater number of sources and sensors on the free surface to enrich the measurement set: there are ten wave sources between $(-45, 0)$ and $(45, 0)$ spaced at 10.0 length units. There are 21 sensors located between $(-100, 0)$ to $(100, 0)$ at a spacing interval of 10.0 units. We employ the frequency-continuation scheme with probing frequencies set at $\omega = 0.1, 0.3, 0.8, 1.3, 1.7, 2.5, 3.3$. As seen in Fig. 12, using the first probing frequency moves the scatterer close to the target (we have again used a shape constraint). Figure 13 depicts the sequence of shape refinements induced by the frequency continuation scheme, whereas Fig. 14 shows the fitness metric convergence. We remark that point (or line) sources cannot illuminate the domain as efficiently as traveling plane waves can, and it thus becomes harder to reconstruct scatterer shapes based on such sources. The problem is exacerbated when non-convex shapes are targeted, especially in the cases considered herein, where all sensors are located in the backscattered region, and therefore are not privy to information emanating from the shadow zone of the scatterers. Still, as the numerical results attest, the shape reconstruction appears quite satisfactory.

5 Conclusions

In this article, we discussed a frequency-domain methodology for detecting the shape and location of rigid scatterers fully embedded within an elastic halfplane, when illuminated by surficial SH line sources. In particular, building upon prior work in the fullplane case, we combined amplitude-based misfits, with continuation schemes, and cast the inverse problem within the general framework of PDE-constrained optimization. We used boundary integral equations to resolve the ensuing Euler-Lagrange optimality conditions, which had resulted in state, adjoint,

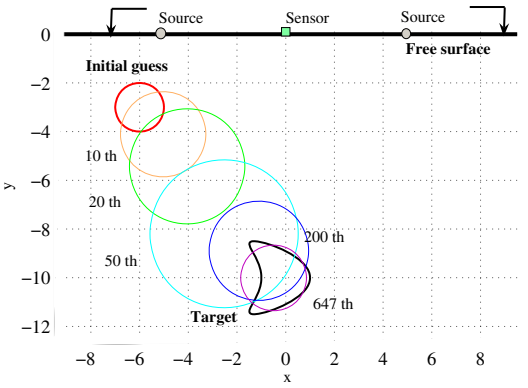

Figure 12: The kite-shaped scatterer: convergence path

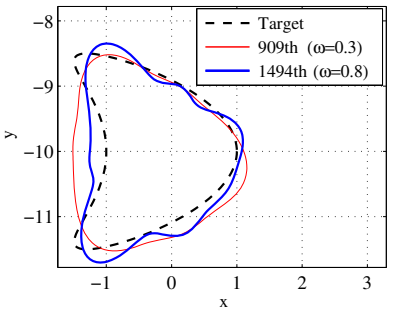

(a) $\omega = 0.3$ and 0.8

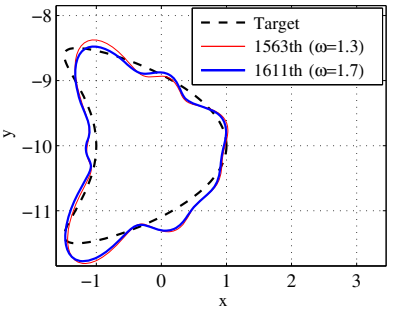

(b) $\omega = 1.3$ and 1.7

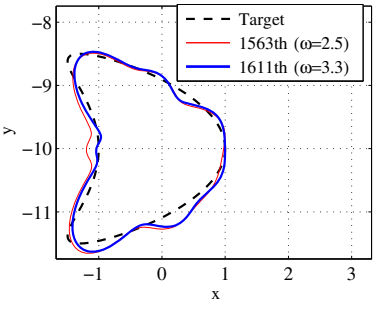

(c) $\omega = 2.5$ and 3.3

Figure 13: The kite-shaped scatterer: convergence stages at $\omega = 0.3, 0.8, 1.3, 1.7, 2.5, 3.3$

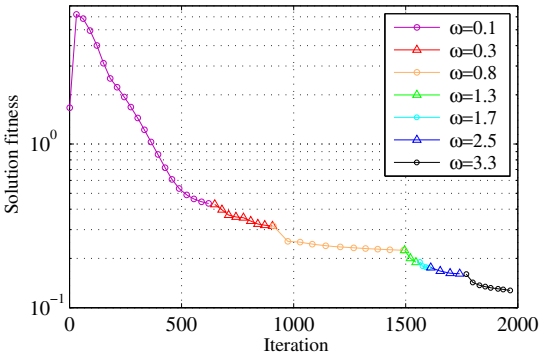

Figure 14: The kite-shaped scatterer: solution-fitness metric

and control problems. In summary, the process has, thus far, exhibited robustness under reasonable (and realistic) configurations of sensors and sources, as evidenced by the numerical results. Despite a relatively large number of iterations needed for convergence, the entire framework is well suited for detection of objects that conform to the assumptions made herein regarding the homogeneity of the background host and the rigidity of the scatterer with respect to the host material. Extensions to the more interesting three-dimensional case are straightforward, albeit computationally more demanding.

Acknowledgement: Partial support for the authors' research presented herein has been provided by the National Science Foundation under grant awards CMS-0348484 and ATM-0325125. This support is gratefully acknowledged.

References

Bonnet, M. (1995): BIE and material differentiation applied to the formulation of obstacle inverse problems. *Engineering Analysis with Boundary Elements*, vol. 15, pp. 121–136.

Colton, D.; Kress, R. (1983): *Integral equation methods in scattering theory*. Wiley-Interscience, New York.

Colton, D.; Kress, R. (1998): *Inverse acoustic and electromagnetic scattering theory*. Springer-Verlag, New York.

Fata, S. N.; Guzina, B.; Bonnet, M. (2003): Computational framework for the BIE solution to inverse scattering problems in elastodynamics. *Computational Mechanics*, vol. 32, pp. 370–380.

Guzina, B.; Fata, S. N.; Bonnet, M. (2003): On the stress-wave imaging of cavities in a semi-infinite solid. *International Journal of Solids and Structures*, vol. 40, pp. 1505–1523.

Harris, S. D.; Mustata, R.; Elliott, L.; Ingham, D. B.; Lesnic, D. (2008): Numerical identification of the hydraulic conductivity of composite anisotropic materials. *CMES: Computer Modeling in Engineering & Sciences*, vol. 25, no. 2, pp. 69–79.

Huang, C.-H.; Shih, C.-C. (2007): An inverse problem in estimating simultaneously the time-dependent applied force and moment of an euler-bernoulli beam. *CMES: Computer Modeling in Engineering & Sciences*, vol. 21, no. 3, pp. 239–254.

Jeong, C. (2006): *Shape detection and localization of a scatterer embedded in a halfplane*. Master thesis, University of Texas at Austin, 2006.

Kirsch, A. (1996): *An introduction to the mathematical theory of inverse problems*. Springer-Verlag.

Kosinski, W. (1986): *Field Singularities and Wave Analysis in Continuum Mechanics*. John Wiley and Sons.

Ling, L.; Takeuchi, T. (2008): Boundary control for inverse cauchy problems of the laplace equations. *CMES: Computer Modeling in Engineering & Sciences*, vol. 29, no. 1, pp. 45–54.

Ling, X.; Atluri, S. (2008): Stability analysis for inverse heat conduction problems. *CMES: Computer Modeling in Engineering & Sciences*, vol. 13, no. 3, pp. 219–228.

Lions, J. L. (1971): *Optimal control of systems governed by partial differential equations*. Springer Verlag, Berlin, Heidelberg, New York.

Marin, L.; Power, H.; Bowtell, R. W.; Sanchez, C. C.; Becker, A. A.; Glover, P.; Jones, A. (2008): Boundary element method for an inverse problem in magnetic resonance imaging gradient coils. *CMES: Computer Modeling in Engineering & Sciences*, vol. 23, no. 3, pp. 149–173.

Na, S.-W. (2006): *On a class of two-dimensional inverse problems: wavefield-based shape detection and localization and material profile reconstruction*. PhD dissertation, University of Texas at Austin, 2006.

Na, S.-W.; Kallivokas, L. F. (2008): PDE-constrained amplitude-based shape detection in inverse acoustic scattering. *Computational Mechanics*, vol. 41, no. 4, pp. 579–594.

Na, S.-W.; Kallivokas, L. F. (2009): Continuation schemes for shape detection in inverse acoustic scattering problems. *CMES: Computer Modeling in Engineering & Sciences (in press)*.

Noroozi, S.; Sewell, P.; Vinney, J. (2006): The application of a hybrid inverse boundary element problem engine for the solution of potential problems. *CMES: Computer Modeling in Engineering & Sciences*, vol. 14, no. 3, pp. 171–180.

Petryk, H.; Mróz, Z. (1986): Time derivatives of integrals and functionals defined on varying volume and surface domains. *Archives of Mechanics*, vol. 38, pp. 697–724.

Tabrez, S.; Mitra, M.; Gopalakrishnan, S. (2007): Modeling of degraded composite beam due to moisture absorption for wave based detection. *CMES: Computer Modeling in Engineering & Sciences*, vol. 22, no. 1, pp. 77–89.

Wu, C.-Y.; Al-Khoury, R.; Kasbergen, C.; Liu, X.-Y.; Scarpas, A. (2007): Spectral element approach for inverse models of 3d layered pavement. *CMES: Computer Modeling in Engineering & Sciences*, vol. 17, no. 3, pp. 163–172.